Research Square

Preprints are preliminary reports that have not undergone peer review.
They should not be considered conclusive, used to inform clinical practice,
or referenced by the media as validated information.

Geochemical and time-lapse electrical monitoring of lead stabilization in shooting-range soil amended with oyster shell and steel slag

Sunjae Lee
Korea Institute of Civil Engineering and Building Technology
Narae Lee
Korea Institute of Science and Technology
Sang-Leen Yun
leen70@kict.re.kr

Korea Institute of Civil Engineering and Building Technology
Jaeyoung Choi
Korea Institute of Science and Technology

Article

Keywords: Soil stabilization, Lead immobilization, Waste oyster shell, Steel slag, Time-lapse electrical resistivity tomography, Induced polarization

Posted Date: November 19th, 2026

DOI: https://doi.org/10.21203/rs.3.rs-11590109/v1

License: This work is licensed under a Creative Commons Attribution 4.0 International License.
Read Full License

Additional Declarations: No competing interests reported.

Geochemical and time-lapse electrical monitoring of lead stabilization in shooting-range soil amended with oyster shell and steel slag

Sunjae Lee[1], Narae Lee[2], Sang-Leen Yun[1*] and Jaeyoung Choi[2*]

[1]Department of Environmental Research, Korea Institute of Civil Engineering and Building Technology, 283 Goyang-daero, Ilsanseo-gu, Goyang-si 10223, Republic of Korea

[2]Center for Climate and Carbon Cycle Research, Korea Institute of Science and Technology, Seoul 02792, Republic of Korea

*Corresponding authors

E-mail: Sang-Leen Yun (Leen70@kict.re.kr); Jaeyoung Choi (Jchoi@kist.re.kr)

Abstract

Although geoelectrical monitoring is not yet routinely used to assess soil solidification/stabilization (S/S), its potential continues to be investigated. In this study, Pb-contaminated soil in a shooting-range mixed with waste oyster shell (O-M) or steel slag (S-M) was monitored against a control (C) for 13 months. Within two weeks, the exchangeable Pb fraction in both amended layers decreased to below 0.2% (C: 8–10%), consistent with pH-driven precipitation and sorption. Diethylenetriaminepentaacetic acid-extractable Pb decreased from 16–17% to 7.4% (O-M) and 2.4% (S-M) of total Pb and toxicity characteristic leaching procedure-extractable Pb to 5.8% and 4.8% (C: 10.2%), indicating progressive conversion into less labile forms, especially with slag. Beneath the amended layers, pH increased by about two units and exchangeable Pb decreased below 0.2%, unlike in the control, suggesting that alkaline constituents leached by rainfall also stabilized Pb there. Time-lapse resistivity and induced polarization imaging revealed changes within and below the amended layers, including persistent resistivity increase beneath both layers and transient normalized-chargeability decrease under drier early-summer conditions. Electrical imaging differentiated the amended zones and their changes, providing a spatially continuous view of stabilization, that together with targeted chemical sampling, can make field S/S assessment more representative.

Keywords: Soil stabilization, Lead immobilization, Waste oyster shell, Steel slag, Time-lapse electrical resistivity tomography, Induced polarization

Introduction

Owing to its persistence, accumulation, and toxicity in soil, lead (Pb) has become an increasing environmental concern worldwide (Bolan et al., 2014; Liu et al., 2018). Outdoor shooting ranges are a major source of soil Pb, because bullets deposited in berms and impact areas gradually weather, releasing Pb and copper (Cu) from the jackets into the surrounding soil over time (Cao et al., 2003a, 2003b; Sorvari et al., 2006). Solidification/stabilization (S/S) is regarded as a practical and cost-effective remediation technology for heavy metal contaminated soils. Rather than removal, S/S reduces contaminants leachability using binding agents that transform mobile and bioavailable metal species into chemically stable and low-soluble forms (Shen et al., 2019; Xu et al., 2021); of which the United States Environmental Protection Agency (US EPA) has recognized as one of the most effective techniques for hazardous waste management (Spence and Shi, 2005; US EPA, 2007). Stabilizing Pb-contaminated shooting-range soils with calcium-rich waste materials, such as eggshell and calcined oyster shell, has been actively investigated in Korea (Ahmad et al., 2012; Moon et al., 2013).

Conventional S/S binders, including Portland cement, lime, phosphates, and geopolymers, have reduced metal mobility with varying success; however, their cost, sustainability, and environmental burden have garnered increasing interest in alternatives derived from waste resources (Jiang et al., 2022; Li et al., 2022). Waste oyster shell (WOS), composed primarily of calcite ($CaCO_3$), increases soil pH through its inherent alkalinity, thereby promoting Pb precipitation as hydroxides or carbonates and its sorption on mineral surfaces (Lee et al., 2008; Ok et al., 2011). In Korea, WOS reuse is supported by the 2021 amendment of the Marine Waste and Marine Sediment Management Act (Choi et al., 2024). Steel slag, an alkaline steelmaking by-product, contains calcium silicates and calcium ferrites that form cementitious hydration products and Fe- and Mn-bearing oxides, which can absorb metals (Yildirim and Prezzi, 2011; Jiang et al., 2022). Steel slag immobilized Pb in laboratory tests (Grubb et al., 2014); and reduced Pb and Cu leachability in a co-contaminated soil, in combination with calcined oyster shell (Moon et al., 2015). Because steel slag and calcined oyster shell differ in their dominant phases, they are expected to retain Pb through different combinations of precipitation, sorption, and encapsulation (Kumpiene et al., 2008), with distinct behaviour under identical field conditions.

Most S/S effectiveness assessments rely on leaching assays such as toxicity characteristic and synthetic precipitation leaching procedures (TCLP and SPLP, respectively), which provide

useful but limited insights into speciation and spatial heterogeneity within treated soils (Xu et al., 2021). Single extractions with diethylenetriaminepentaacetic acid (DTPA) and Mehlich-3 offer complementary information on the potentially bioavailable fraction, and sequential extraction protocols such as the Tessier method enable metal redistribution among fractions of different mobility to be followed (Tessier et al., 1979). However, these chemical methods are destructive, not representative of the sampling area, and unable characterize the physical state of the entire treated zone (Ahn et al., 2020). Moreover, these methods are usually repeated a few times, although stabilization reactions continue to evolve for long after amendment (Bian et al., 2014; Cui et al., 2016); therefore, evaluations based on a single sampling event or amended layer alone may misrepresent the extent and durability of stabilization.

Electrical resistivity tomography (ERT) and induced polarization (IP) can complement these analyses as non-invasive S/S in-situ evaluation tools (Saneiyan et al., 2018; Martinho, 2023). Resistivity is sensitive to porosity, pore-water ionic strength, and water content, each of which can be altered by amendment-induced reactions, whereas IP responds to polarization at mineral–fluid interfaces, which is affected by mineral precipitation and ion adsorption (Slater and Lesmes, 2002; Revil et al., 2012). In laboratory studies, stabilized soils resistivity increased with hydration and correlated with Pb leachability (Chen et al., 2011; Liu et al., 2021); resistivity and IP were monitored together with long-term leaching in a steel slag-stabilized As-contaminated soil (Lee et al., 2023), and laboratory IP measurements tracked metal uptake by reactive materials, with a direction of change that depended on the reaction products. Calcite precipitation reduced polarization in zero-valent iron columns (Wu et al., 2008) and calcite conversion into Pb carbonate lowered the normalized chargeability (M_N) (Yang et al., 2024), whereas Pb retention on activated carbon increased the imaginary conductivity (Hao et al., 2021) and the response to Cu sorption on biochar depended on the Cu concentration (Zhou et al., 2024). S/S field applications remain at early stages: a recent review of electrical methods for in-situ remediation assessment focused on chemical oxidation and reduction, bioremediation, thermal treatment, and permeable reactive barriers (Xia et al., 2026), and most studies relating IP to amendment–metal interactions have been conducted at laboratory scale (Hao et al., 2021; Song et al., 2026). In a field trial, chargeability was elevated in a powdered WOS layer immediately after application and increased over nine months in a granular WOS layer (Lee et al., 2025a). Repeated surveys of

amendments with contrasting mineralogy under the same field conditions can further clarify how the electrical response of stabilized soil depends on the amendment and its reactivity.

In this study, WOS and steel slag were each mixed at 5% (w/w) with Pb-contaminated soil and placed as a 0.3-m-thick layer over untreated contaminated soil in field plots at a former military shooting range in Yeoju, Republic of Korea, alongside an unamended control plot. The plots were monitored on three occasions over approximately 13 months. The study objectives were to: (i) compare the changes in Pb leachability (TCLP), extractability (Mehlich-3 and DTPA) and fractionation (Tessier method) produced by the two amendments in the amended layer and the underlying contaminated soil; (ii) characterize the evolution of resistivity and M_N in the amended plots using time-lapse ERT and time-domain IP (TDIP), referenced to the first post-construction survey; and (iii) examine the correspondence between the electrical images and the geochemical changes in the amended layer and the underlying contaminated soil, and thereby show how electrical surveys can guide sampling in the field monitoring of S/S with waste-derived amendments.

Results and Discussion

Steel slag and amended soils properties

As per our previous field study, WOS consisted of calcite, with CaO and CO_2 contents of approximately 41.0 and 45.9 wt%, respectively; whereas steel slag exhibited a more complex mineralogy (Fig. 2). Its XRD pattern contained reflections of wüstite (FeO), brownmillerite ($Ca_2(Fe,Al)_2O_5$), calcite ($CaCO_3$), larnite (β-Ca_2SiO_4) and magnetite (Fe_3O_4) (Fig. 2a). The most intense reflection, at a 2θ of approximately 29.4°, was assigned to calcite, and distinct wüstite reflections appeared at approximately 36.1°, 42.0°, and 60.9°, whereas the reflections of brownmillerite, larnite and magnetite overlapped between 32° and 36°. Dicalcium silicate (larnite), brownmillerite, and wüstite are phases typical of steelmaking slag (Yildirim and Prezzi, 2011), and magnetite is an additional Fe-bearing constituent. Dicalcium silicate hydration yields calcium silicate hydrate and $Ca(OH)_2$ (Taylor, 1997), which can supply alkalinity and form cementitious products, while weathered Fe-oxide surfaces may provide sorption sites for Pb (Kumpiene et al., 2008).

Consistent with the XRD results, CaO (43.8 wt%) and Fe_2O_3 (31.6 wt%, total Fe expressed as Fe_2O_3) were the principal constituents of the slag, followed by SiO_2 (10.4 wt%), MnO and MgO (3.3 wt% each), and P_2O_5 and Al_2O_3 (2.3 wt% each) (Fig. 2b). Unlike the WOS, which consisted mostly of CaO and CO_2, the slag contained Ca in silicate, ferrite and carbonate

phases together with substantial Fe and Mn. The two amendments were therefore expected to differ both in the rate at which they release alkalinity and in solid phases available for Pb retention.

Both the amended and unamended soils were classified as sandy loam, indicating that the amendments did not change the soil texture (Table 1). In contrast, soil pH and EC differed significantly among the plots at T_1. In the 0–30 cm layer, pH was 4.76 in C but 7.58 in O-M and 9.98 in S-M, and EC increased from 1,645 μS cm^{-1} in C to 7,615 and 9,840 μS cm^{-1} in O-M and S-M, respectively. In O-M, these increases reflect calcite dissolution, which consumes protons and releases Ca^{2+} and carbonate species (Ok et al., 2011). The higher pH in S-M is consistent with the $Ca(OH)_2$ released by calcium silicates hydration and any free lime in the slag, which increases soil solution pH above the range buffered by calcite. At 60 cm, pH (6.31 and 6.72) and EC (2,235 and 3,115 μS cm^{-1}) in O-M and S-M, respectively, were also higher than in C (5.52 and 1,150 μS cm^{-1}), although the differences were much smaller than in the amended layer, suggesting commencement of solutes infiltration from the overlying layer during the two weeks after placement.

The TOC content of the O-M amended layer (3.97%) was higher than that of C (2.44%) (Table 1), consistent with the increase in soil organic matter reported after oyster shell application (Lee et al., 2008). Total Pb differed among the plots, depths and sampling dates (Table 1; Supplementary Table S3), as expected for point samples from contaminated soil in which Pb is distributed heterogeneously. As contents measured at different sampling points are difficult to compare directly, extractable Pb was expressed as a percentage of the total Pb of the same sample, providing a common basis for comparing the different extraction methods results.

Changes in Pb extractability in the amended layer and underlying soil

SPLP-extractable Pb was below the lowest calibration standard (0.1 mg L^{-1}) in 16 of the 18 samples and did not exceed a mean of 0.12 mg L^{-1} (≤ 0.10% of total Pb) in any sample (Supplementary Table S3); its comparison therefore focuses on TCLP, Mehlich-3, and DTPA (Fig. 3).

In C, TCLP-extractable Pb in the 0–30 cm layer varied by 0.24 percentage points (pp) over the monitoring period (10.24–10.48%; Fig. 3a), representing temporal variation in the absence of an amendment. Against this baseline, both amended layers released less Pb than C from the first sampling onward, by 3.49–4.45 pp in O-M and 4.63–5.66 pp in S-M, and

TCLP-extractable Pb decreased from 6.85 to 5.80% in O-M and from 5.71 to 4.84% in S-M by T_3. Mehlich-3-extractable Pb in C varied between 29.69 and 35.98% (Fig. 3b). In O-M, it was similar to that in C at T_1 (28.95%) but decreased to 27.79% at T_2 and 21.69% at T_3, whereas S-M yielded the lowest values throughout (13.72–18.89%); the slight increase in S-M between T_2 and T_3 (from 13.72 to 16.05%) was smaller than the temporal variation in C (6.29 pp). DTPA-extractable Pb in the amended layers was close to that in C at T_1 (16.62% in O-M and 16.07% in S-M vs 16.90% in C; Fig. 3c), but decreased sharply to 9.45 and 2.11% at T_2 and to 7.42 and 2.41% at T_3, whereas C varied only between 16.90 and 19.51% for O-M and S-M, respectively. The reductions at T_3 (11.39 and 16.40 pp) corresponded to 61 and 87% of the control value. Mehlich-3, a composite reagent of weak acids and a chelating agent, can extract the exchangeable, carbonate-bound and part of the Fe/Mn oxide-bound metal, whereas DTPA at near-neutral pH mainly removes the exchangeable and part of the organically complexed metal (Yu et al., 2004; Feng et al., 2005; Farshadirad et al., 2017), which explains the higher extraction yields of Mehlich-3.

The different timing of the TCLP and DTPA responses indicates that the two tests captured different aspects of stabilization. The early reduction in TCLP-extractable Pb coincided with the elevated pH of the amended layers, which lowered Pb solubility; furthermore, alkaline materials buffer the acetic acid extraction fluid, and the final leachate pH largely controls metal leachability in the TCLP (Halim et al., 2003). Because the DTPA extractant is buffered at pH 7.3, it is less affected by soil alkalinity, and its delayed decrease suggests that Pb in the amended layers was progressively transformed into less labile forms during the months after placement. At T_1, DTPA-extractable Pb in the amended layers (16.07–16.62%) exceeded the sum of the exchangeable and organic-bound fractions (0.10–5.75% of the fractionated Pb; Fig. 4c), indicating that the chelating extractant also accessed Pb assigned by the sequential extraction to other fractions, such as freshly formed precipitates or weakly sorbed species. In the S-M layer at T_2 and T_3, TCLP-extractable Pb (4.8%) exceeded DTPA-extractable Pb (2.1–2.4%), the reverse of the order in C (10–11% vs 17–20%), which indicates that part of the Pb retained by the slag remained soluble under acidic TCLP conditions. The progressive decrease in DTPA-extractable Pb supports field studies in which the effects of amendments on metal availability persisted or strengthened over several years (Bian et al., 2014; Cui et al., 2016).

Within the amended layer, S-M consistently produced higher reductions. The higher pH of the slag-amended layer at T_1 (9.98 vs 7.58) supports the hydrolysis of Pb^{2+} and its

precipitation as hydroxides and hydroxycarbonates (Porter et al., 2004), and the hydration products of the slag can retain Pb through sorption, precipitation, and incorporation (Chen et al., 2009), which may explain why S-M retained the lower extractability at T_2 and T_3, when both amended layers had a similar pH of 8.7–8.9 (Fig. 4a). In O-M, the reaction between calcite and dissolved Pb may be partly self-limiting, because dissolved Pb^{2+} can inhibit calcite dissolution through Pb-bearing surface layer formation (Abdilla et al., 2024).

At 60 cm, where the soil had not been mixed with the amendments, extractable Pb at T_1 was similar among TCLP (10.11–11.22%) and DTPA (19.83–20.99%) plots, whereas Mehlich-3-extractable Pb was higher in O-M (35.97%) and S-M (31.99%) than in C (26.90%) (Fig. 3d–f). In C, TCLP-, and DTPA-extractable Pb varied within 0.64 pp (11.22–11.86%) and 3.40 pp (19.40–22.80%) at this depth, respectively, and Mehlich-3-extractable Pb increased from 26.90 to 32.10%. In both amended plots, by contrast, extractable Pb decreased: between T_1 and T_3, TCLP-extractable Pb declined from 10.11 to 6.63% in O-M and from 10.41 to 4.23% in S-M, and Mehlich-3-extractable Pb fell to 22.85% and 17.63%, respectively (Fig. 3d, 3e). DTPA-extractable Pb decreased to 9.62% in O-M and 6.57% in S-M at T_2; at T_3, it decreased further to 7.69% in O-M, whereas in S-M it increased to 14.24%, remaining below the values in C (Fig. 3f).

Because the 60-cm soil received no amendment, these decreases suggest that the influence of the amended layers extended into the underlying contaminated soil within the first year, and the concurrent increases in pH and EC at this depth (Fig. 4d, 4e) are consistent with alkalinity and dissolved ions being carried downward by infiltrating rainwater.

The large reductions in the amended layers reflect the large labile Pb pool of this soil, in which DTPA extracted 17–23% of total Pb and the exchangeable fraction accounted for 8–10% in C (Fig. 4c, 4f). The greater effectiveness of the slag correlates with the immobilization of Pb by steel slag fines (Grubb et al., 2014) and with the lower Pb and Cu leachability obtained with steel slag combined with calcined oyster shell (Moon et al., 2015). Because S/S immobilizes Pb rather than removing it, part of the acid-leachable Pb remained: at T_3, TCLP-extractable Pb was 43% (O-M) and 53% (S-M) lower than in C, but the leachates still contained 11.07 and 8.64 mg L^{-1} of Pb, above the US EPA toxicity characteristic level of 5.0 mg L^{-1} (US EPA, 40 CFR 261.24). This suggests that a higher amendment dose would be required to meet criterion in soils as contaminated as the study area.

Changes in soil pH, EC, and Pb fractionation

In the 0–30 cm layer of C, pH changed little over the monitoring period (4.76–5.08), whereas both amended layers remained alkaline, at pH 8.71–8.91 at T_2 and T_3 (Fig. 4a). EC in the amended layers decreased from the T_1 values but remained higher (5,485–6,025 µS cm^{-1} in O-M and 6,510–7,525 µS cm^{-1} in S-M at T_2 and T_3) than in C (1,130–1,645 µS cm^{-1}) (Fig. 4b), consistent with the gradual leaching of soluble salts by infiltrating rainwater.

At 60 cm, pH increased from 6.31 to 8.05 and 8.57 in O-M and from 6.72 to 8.61 and 8.60 in S-M, whereas it varied between 4.41 and 5.52 in C (Fig. 4d); the soil below the amended layers thus became about two pH units more alkaline, whereas the control soil did not. EC at this depth increased temporally in O-M (from 2,235 to 3,245 µS cm^{-1}) and more strongly in S-M (from 3,115 to 6,855 µS cm^{-1}), but not in C (1,030–1,665 µS cm^{-1}) (Fig. 4e). These trends suggest that alkalinity and solutes moved from the amended layers into the underlying soil, in correlation with the decreases in extractable Pb at 60 cm (Fig. 3d–3f).

The Tessier sequential extraction provides chemical evidence for the stabilization mechanisms (Fig. 4c, 4f). In the 0–30 cm layer of C, Pb was distributed as F5 (60.9–67.6%) > F3 (15.0–20.4%) > F1 (8.2–10.2%) ≥ F2 (6.1–8.0%) > F4 (1.3–2.5%) throughout the monitoring period, indicating no systematic change in Pb speciation in the absence of an amendment. In both amended layers, by contrast, the exchangeable fraction was almost absent from T_1 onward (0.02–0.14% of the fractionated Pb, or 0.8–6.1 mg kg^{-1} compared with 285–345 mg kg^{-1} in C). The near-complete loss of exchangeable Pb within two weeks of placement is consistent with the rapid pH increase, which promotes the hydrolysis of Pb^{2+} and its precipitation or specific adsorption on mineral surfaces (Porter et al., 2004).

In O-M, the carbonate-bound proportion was already much higher than in C at T_1 (16.41% vs 6.12%, or 540 vs 171 mg kg^{-1}), and increased to 17.97% at T_2 and 23.26% at T_3. The elevated F2 from the first sampling, together with the near-absence of F1, suggests that exchangeable Pb was rapidly converted into carbonate-associated forms, such as cerussite ($PbCO_3$) or Pb sorbed on calcite surfaces, by reaction with the carbonate supplied by the dissolving shell calcite; calcite dissolution has been shown to drive Pb immobilization through carbonate precipitation in laboratory studies (Xue et al., 2023).

In S-M, F5 dominated at T_1 (78.75%) and T_3 (82.64%), whereas F2 and F3 increased to 18.01% and 29.45%, respectively, at T_2, and F5 decreased to 51.88%. The high proportion of F5 may partly reflect Pb retained within slag-derived hydration products that resisted the

reagents of the first four extraction steps (Chen et al., 2009), and the transient increase in F3 may indicate Pb association with Fe and Mn (hydr)oxides derived from the slag. Consequently, DTPA-extractable Pb remained low at T_2 and T_3 (2.11% and 2.41%; Fig. 3c), indicating that the labile Pb pool in S-M was consistently suppressed despite the shifts among F2, F3, and F5.

At 60 cm, the exchangeable fraction in C remained at 8.22–8.72%, whereas it decreased in O-M from 8.51% at T_1 to 5.66% at T_2 and 0.10% at T_3 (from 420 to 1.9 mg kg^{-1}) and in S-M from 7.21% to 0.81% and 0.17% (from 443 to 4.0 mg kg^{-1}) (Fig. 4f). Over the same period, the proportion of F2 increased from 6.88 to 29.90% in O-M and 7.61 to 20.92% in S-M, while only varying in C between 5.84 and 7.07%; in absolute terms, F2 increased in O-M from 340 to 557 mg kg^{-1} and in S-M from 467 to 748 mg kg^{-1} at T_2. The shift from exchangeable to carbonate-bound Pb below the amended layers coincided with the pH increase at this depth (Fig. 4d), supporting the interpretation that alkaline solutions derived from the amendments migrated into the underlying soil and promoted Pb immobilization there; the faster decline of F1 in S-M, almost complete by T_2, is consistent with the higher pH and EC of the slag-derived solutions.

Collectively, the decrease in F1 and increase in F2 in the O-M amended layer and soil below both amended layers indicate a transfer of Pb from exchangeable to carbonate-associated forms, as reported for a Korean shooting-range soil amended with eggshell, in which exchangeable Pb decreased to about 1% of total Pb while carbonate-associated Pb increased (Ahmad et al., 2012). The lower F1 and TCLP-extractable Pb in the amended layers than in C from T_1 onward, together with the subsequent decrease in DTPA-extractable Pb in these layers and the decreases in F1 and in TCLP- and Mehlich-3-extractable Pb at 60 cm between T_1 and T_3, provide consistent chemical evidence that both amendments reduced Pb mobility within the amended layers and underlying soil.

Electrical resistivity responses

Geophysical surveys complemented the point-based chemical analyses by tracking spatial and temporal evolution of the amended plots without soil disturbance (Figs. 5–7). As no survey was made in C, amendment-related changes were evaluated by comparing the amended layer (0–0.3 m) with the underlying soil within each section and by comparing the two plots, which were surveyed on the same dates and are displayed on common colour scales.

At T_1, the O-M section displayed a conductive zone near the surface (median 64.8–101.9 Ω m in the upper 0.3 m) that graded downward into the contaminated soil, where resistivity increased from 110.8 Ω m at 0.3–0.4 m to 234.0 Ω m at 0.7–0.8 m (Figs. 5a and 7a). No comparable zone was found in S-M, where resistivity ranged from 144.3 to 277.5 Ω m, with a relatively resistive band at 0.1–0.2 m and the lowest values at 0.3–0.4 m (Figs. 5b and 7b). The conductive upper O-M section is consistent with the increased pore-water ionic strength caused by calcite dissolution (EC 7,615 μS cm^{-1}) and with the higher water content of this layer (20.3% vs 13.3% in C; Supplementary Table S1), both of which enhance electrolytic conduction (Merritt et al., 2016). The absence of such a zone in S-M despite its higher EC (9,840 μS cm^{-1}) indicates that factors other than soluble salts also influenced the bulk resistivity of the slag-amended soil, such as its lower water content (17.3%) and early hydration of the slag, which can increase resistivity by decreasing porosity (Chen et al., 2011; Liu et al., 2019).

Resistivity in O-M increased temporally throughout the section. At T_2, the median T_2/T_1 ratios were 1.61–1.75 in the amended layer and 1.52–2.22 below it, increasing with depth (Figs. 5c and 7e). By T_3, the ratios had decreased to 1.19–1.37 at 0.1–0.3 m and 1.18–1.44 below the amended layer, whereas the ratio at 0–0.1 m (1.65) remained similar to that at T_2 (Figs. 5e and 7e). In S-M, resistivity at T_2 decreased near the surface (median ratio of 0.81 at 0–0.1 m) but increased by factors of 1.40–1.96 between 0.1 and 0.8 m (Figs. 5d and 7f). At T_3, the S-M section showed changes of opposite sign above and below the base of the amended layer: resistivity in the upper 0.3 m decreased to 0.55–0.84 of its T_1 value, whereas below 0.3 m it increased to 1.15–1.89 times the T_1 value, with the ratio rising with depth (Figs. 5f and 7f).

Resistivity increase in the O-M amended layer coincided with decreases in EC (from 7,615 to 5,485–6,025 μS cm^{-1}) and water content (from 20.3% to 14.4% at T_2 and 16.4% at T_3), both of which reduce electrolytic conduction (Merritt et al., 2016), and the precipitation of dissolved ions, for example as carbonates, would further lower the concentration of charge carriers and can clog pores (Wu et al., 2010). In contrast, resistivity decrease in the S-M amended layer at T_3 occurred although its water content (12.2% vs 17.3%) and EC (6,510 vs 9,840 μS cm^{-1}) were lower than at T_1. Moisture and soluble salts alone therefore are limited in explaining this response, which may also reflect changes in the solid phase of the slag-amended layer: the hydration of slag-derived calcium silicates forms calcium silicate hydrate

with a large specific surface area (Taylor, 1997), and surface conduction along such surfaces can contribute substantially to bulk conductivity (Revil and Glover, 1998).

Below the amended layers, resistivity at T_3 remained higher than at T_1 in both plots (ratios of 1.18–1.44 in O-M and 1.15–1.89 in S-M), although EC at 60 cm had increased and the water content was similar to that at T_1 (17.4% vs 18.6% in O-M and 17.6% vs 16.7% in S-M). Because more soluble salts would decrease resistivity, these increases may reflect a change in the pore structure of the underlying soil, such as the partial filling of pores by newly formed precipitates that reduces the connectivity of the conductive pore network (Liu et al., 2019; Wu et al., 2010), consistent with the shift from exchangeable to carbonate-bound Pb at 60 cm (Fig. 4f).

Normalized chargeability responses

At T_1, M_N was highest in the upper 0.5 m of O-M (median 0.017–0.024 mS m^{-1}) and decreased with depth to 0.009 mS m^{-1} (Figs. 6a and 7c), whereas in S-M it was lower in the amended layer (0.010–0.017 mS m^{-1}) and peaked at 0.3–0.4 m (0.024 mS m^{-1}), immediately below the amended layer (Figs. 6b and 7d). The elevated M_N in the upper O-M section is consistent with the addition of fine calcite particles, which increases the interfacial area per unit pore volume that controls polarization (Slater et al., 2006; Weller et al., 2010). The lower M_N of the S-M layer suggests that the slag did not enhance polarization at this stage despite its Fe-bearing phases, in line with the lower chargeability of a layer stabilized with 3% steelmaking slag than of the overlying topsoil in a field pilot (Ahn et al., 2022). The maximum just below the S-M layer may reflect slag-derived solutes accumulating at the interface, because the quadrature conductivity increases with pore-water salinity (Revil and Skold, 2011), in correlation with the higher EC at 60 cm in S-M than in C at T_1.

M_N decreased at T_2 in both plots but with different depth patterns (Figs. 6c, 6d and 7g, 7h). In O-M, the median ratio was 0.58–0.69 in the upper 0.4 m and 0.79–0.82 between 0.4 and 0.8 m, whereas in S-M it decreased only moderately in the amended layer (0.66–0.89) but strongly below it (0.37–0.49 between 0.3 and 0.8 m). At T_3, M_N in O-M partly recovered in the upper 0.6 m (ratios of 0.78–1.16) and exceeded the T_1 values toward the base of the section (1.20–1.59 at 0.6–0.8 m) (Figs. 6e and 7g). In S-M, M_N at T_3 increased in the upper 0.2 m (1.46–1.52) and partly recovered below 0.3 m, where the ratio rose with depth from 0.78 to 1.12 (Figs. 6f and 7h).

The general decrease in M_N at T_2 coincided with the lowest water contents of the monitoring period (Supplementary Table S1). Because the polarization of unsaturated soils depends on water saturation, and M_N decreased with drying in clay-bearing sand mixtures (Breede et al., 2012), drying may have contributed to the decrease in both plots. However, the decrease below the S-M layer (0.37–0.49) was more than in O-M at the same depths (0.69–0.82), although the water content at 60 cm decreased less in S-M (from 16.7 to 13.1%) than in O-M (from 18.6 to 12.6%). Between T_1 and T_2, pH at 60 cm in S-M increased from 6.72 to 8.61 and the exchangeable fraction decreased from 7.21 to 0.81% (Fig. 4d, 4f), so the chemical changes below the slag layer occurred mainly during this interval. Because calcite precipitation on zero-valent iron grains reduced polarization (Wu et al., 2008) and the conversion of calcite into Pb carbonate lowered M_N (Yang et al., 2024), the coating of grain surfaces by precipitates formed from slag-derived solutions may have reduced interfacial polarization below the S-M layer. As M_N partly recovered by T_3, when the water content had returned to T_1 level, T_2 response probably reflected the combined effects of drying and chemical change; separating these effects will require complementary measurements, such as laboratory calibration of the moisture dependence of M_N for the site soil and mineralogical analysis of the precipitates.

Because M_N is obtained by dividing m by ρ, its increase in the upper 0.2 m of S-M at T_3 largely mirrored the resistivity decrease in this zone. The increase toward the base of the O-M section at T_3 coincided with the EC increase at 60 cm (from 2,235 to 3,245 $\mu S\ cm^{-1}$) and may reflect the arrival of solutes from the amended layer, which increases the quadrature conductivity (Revil and Skold, 2011).

Unlike laboratory columns, in which pore-water composition and saturation are controlled, field measurements are additionally affected by seasonal variations in soil moisture, so the moisture state at the time of each survey is an important factor in interpreting field IP responses (Ulrich and Slater, 2004); in a slag-stabilized field pilot, the chargeability of the stabilized soil likewise varied with water content (Ahn et al., 2022). Because wüstite and magnetite are electronically conductive or semiconductive, part of the S-M response may also involve the polarization of slag particles, which has been reported to be difficult to distinguish from interfacial polarization at silicate and carbonate surfaces because both scale with the surface area of the polarizable grains (Slater et al., 2006).

Depth-resolved comparison of geophysical and geochemical changes

The depth profiles in Fig. 7 summarize the vertical structure of these changes in the central part of each section (1.0–2.8 m along A–A′), where the model cells cover the full 0–0.8 m depth range; the shaded bands represent the lateral variability of the cells in each 0.1 m interval rather than measurement uncertainty. In S-M, the T_3/T_1 resistivity ratio changed from below 1 to above 1 between the 0.2–0.3 m interval (0.84) and the 0.3–0.4 m interval (1.15), which corresponds to the base of the amended layer (Fig. 7f). Although the layer boundary was not imposed in the inversion, the resistivity changes delineated the amended layer and the underlying soil as zones that changed in opposite directions, whereas in O-M the ratio profiles were more uniform with depth (Fig. 7e).

Both data sets indicate that the amendments effects were not confined to the amended layers: at 60 cm, pH increased by about two units, exchangeable Pb decreased to ≤ 0.17% and TCLP-extractable Pb decreased by 3.48 and 6.18 pp in O-M and S-M between T_1 and T_3, respectively, whereas no such changes occurred in C; and over the same depth range resistivity increased in both sections and M_N below the S-M layer decreased transiently (Figs. 3d, 4d, 4f and 7e–h). In Pb-contaminated soil solidified with a slag-based binder, resistivity increased with curing time, while leached Pb decreased (Liu et al., 2021). The concurrent increase in resistivity and decrease in TCLP-extractable Pb below the amended layers are consistent with this relationship, whereas the resistivity of the S-M amended layer was additionally influenced by the solid-phase changes discussed above.

These observations have two implications for the monitoring of S/S sites. First, the electrical responses were amendment-specific and non-monotonic. The reversal of the S-M changes between T_2 and T_3 would not have been detected by a single post-application survey, and the three-survey design separated a transient change (the T_2 decrease in M_N) from a persistent one (resistivity increase below the amended layers). Second, time-lapse electrical imaging identified the spatial distribution of the subsurface changes, including those occurring beneath the amended layers, which sampling of the amended layer alone would have missed. These observations provide an indirect but spatially continuous representation of the treated profile. When used in identifying zones of change and selecting target locations, chemical and mineralogical analyses, such as XRD and scanning electron microscopy, can establish the nature of the changes. Integrating these analytical methods enables accurate interpretations of subsurface evolution than either method alone. Electrical imaging is increasingly used in this

manner to support the assessment of remediation performance (Lévy et al., 2022; Xia et al., 2026).

Conclusion

This study evaluated Pb stabilization in a shooting-range soil amended with WOS or steel slag at 5% (w/w) in field plots monitored over 13 months, by combining single and sequential extractions with time-lapse ERT and TDIP. Both amendments removed the exchangeable Pb fraction from the amended layer within two weeks of placement (from 8–10% in C to below 0.2%) and lowered TCLP- and DTPA-extractable Pb relative to C, with the slag producing the highest reductions; at T_3, DTPA-extractable Pb accounted for 2.41% of total Pb in S-M and 7.42% in O-M, compared with 18.81% in C. The decrease in DTPA-extractable Pb developed temporally after the initial pH increase, indicating continued transformation of Pb into less labile forms. The stabilizing effect also extended into the underlying contaminated soil, where pH increased by about two units, the exchangeable fraction decreased to ≤ 0.17% and TCLP-extractable Pb decreased by 3.48–6.18 pp, whereas C remained unchanged, suggesting that amendment-derived alkalinity migrated downward with infiltrating water. Because the TCLP leachates of both amended layers still exceeded the US EPA toxicity characteristic level for Pb, higher doses should be considered for soils containing several thousand milligrams of Pb per kilogram.

Time-lapse ERT and TDIP illustrated these changes without disturbing the soil: the WOS-amended layer was initially conductive and became more resistive, with resistivity increasing beneath both amended layers where Pb was transferred to less mobile forms, and the slag-amended plot showing a transient M_N decrease below the amended layer and contrasting resistivity changes above and below the base of the layer. The electrical images thus delineated the amended layers, the underlying soil affected by the amendments and the timing of their changes, information that point sampling alone does not provide. A monitoring procedure in which repeated electrical surveys identify zones of change and guide targeted sampling for chemical and mineralogical analyses can therefore provide a more complete assessment of field S/S performance than either approach alone.

Materials and methods

Site description and test plot design

The study site is a former military shooting range in Yeoju-si, Gyeonggi Province, Republic of Korea (Fig. 1a), which was operated until the early 2000s and has since been abandoned. Pb-contaminated soil at this range—caused by heavy metals accumulation in the surface soil, particularly Pb and Cu, from long-term shooting activities—was previously estimated from geochemical and geophysical data (Lee et al., 2025b). As a military facility, the site belongs to Region 3 under the Korean Soil Environment Conservation Act. In the previous sampling event, total Pb in the test plots soils ranged 3,007–6,015 mg kg^{-1} for all samples, exceeding Region 3 soil contamination threshold (2,100 mg kg^{-1}), above which remediation is required; in contrast to total Cu, which averaged 403 mg kg^{-1} before plot construction (n = 8) and remained far below the corresponding standard (6,000 mg kg^{-1}) (Table 1; Ministry of Environment of Korea, 2018). Pb exceedance justified the installation of field-scale stabilization plots at this location. Test-plot construction, soil sampling and geophysical surveys at the site were carried out with permission from the Ministry of National Defense, Republic of Korea.

Three test plots were constructed at the end of August 2021 to compare the stabilizing agents (Fig. 1b–d): (i) oyster shell-mixed plot (O-M); (ii) control plot (C), containing only contaminated soil; and (iii) steel slag-mixed plot (S-M). O-M and S-M each measured 4 × 2 × 1 m and C measured 2 × 2 × 1 m; all plots were enclosed by 14.5-mm-thick waterproof plywood walls. In O-M and S-M, contaminated soil was first placed to a depth of 0.7 m. Contaminated soil was then mixed on site with the respective stabilizer at 5% of the field-moist soil weight and placed on top as a 0.3-m-thick layer (Fig. 1d), and water was sprayed onto this layer to accelerate early reactions such as hydration. C was filled with contaminated soil only to a depth of 1 m and served as the reference for chemical monitoring.

Stabilizing agents

The WOS was the same material as that prepared and characterized in our previous field study (Lee et al., 2025a). Briefly, shells collected from a seafood market in Tongyeong, Republic of Korea, were rinsed with tap water followed by distilled water, dried at 95 °C for 8 h and subsequently at 105 °C for 72 h, reduced to below 2 mm with a hammer crusher and ground to 100–1,000 μm with a ball mill crusher, and the resulting powder was used in this study. The steel slag, a by-product of steelmaking, was used as particles finer than 2 mm. Its

crystalline phases were determined by X-ray diffraction (XRD) using a Bruker D2 Phaser diffractometer (Bruker Corporation, Billerica, MA, USA) with Cu-Kα radiation (λ = 1.5406 Å), and its elemental composition was assessed by X-ray fluorescence (XRF) spectroscopy using a Rigaku ZSX Primus II spectrometer (Rigaku Corporation, Tokyo, Japan) under the same conditions as in that study; both analyses were performed on the fraction passing a 100-mesh sieve.

Soil sampling and physicochemical analyses

Soil sampling and geophysical surveys were conducted on the same days on three occasions: 15 September 2021 (T_1, approximately two weeks after plot construction), 14 June 2022 (T_2, 272 days after T_1) and 17 October 2022 (T_3, 397 days after T_1). On each occasion, one sample was collected from the 0–30 cm layer and another from 60 cm-depth in each plot; in O-M and S-M plots, these samples represented the amended and underlying contaminated soil layers, respectively. Samples were taken with an Edelman auger (Eijkelkamp, Netherlands) and sealed in polyethylene bags, which were kept cool and delivered to the laboratory within approximately 1 h to minimize physicochemical property changes of the soil. Gravimetric water content was determined in duplicates on the field-moist samples by oven drying at 105 °C (Supplementary Table S1), and the remaining soil was air-dried and passed through a 2-mm sieve before analysis.

Soil pH was measured in a 1:5 (w/v) suspension with deionized water using a glass electrode pH meter (Manufacturer, City, Abb. State, Country), and electrical conductivity (EC) was determined in the same suspension with a conductivity meter (Orion Star A212: Thermo Fisher Scientific, Waltham, MA, USA); both were measured in duplicate. Particle-size distribution was determined by the hydrometer method and classified according to the United States Department of Agriculture (USDA) system, and total organic carbon (TOC) was determined by the Walkley–Black dichromate oxidation method.

Chemical evaluation of stabilized soils

Six methods were applied to determine Pb concentrations and chemical forms in the soil samples. Total metal contents were determined by aqua regia digestion following ISO 11466, with quantification by inductively coupled plasma optical emission spectrometry (ICP-OES; Agilent Technology, 730 Axial). Leachability was evaluated using modified versions of the TCLP (US EPA Method 1311) and SPLP (US EPA Method 1312), which simulate leaching under acidic landfill conditions and by acid rain, respectively; the sample mass was reduced

to 5.0 g, while the extraction fluids, the liquid-to-solid ratio (20 L kg^{-1}) and the agitation time (18 h) of the original methods were retained, followed by filtration and ICP-OES analysis. Plant-available fractions of Pb were assessed using Mehlich-3 (0.2 M CH_3COOH + 0.25 M NH_4NO_3 + 0.015 M NH_4F + 0.013 M HNO_3 + 0.001 M ethylenediaminetetraacetic acid (EDTA), pH 2.5) and DTPA (0.005 M DTPA + 0.01 M $CaCl_2$ + 0.1 M triethanolamine, pH 7.3) extractions. To assess the chemical forms of Pb, the five-step Tessier sequential extraction procedure (Tessier et al., 1979) was used to fractionate Pb into exchangeable (F1), carbonate-bound (F2), Fe/Mn oxide-bound (F3), organic-bound (F4) and residual (F5) forms.

Extracted Pb was expressed as a percentage of the total Pb of the same sample (% of total), with TCLP and SPLP concentrations converted to a soil-mass basis using the liquid-to-solid ratio of 20 L kg^{-1}, and Tessier fractions were expressed as percentages of the sum of F1–F5. Before sample analysis, the ICP-OES was calibrated with standards of 0, 0.1, 0.5, 1, 5 and 10 mg L^{-1} prepared from high-purity ICP multi-element standard solution IV (Certipur, Sigma-Aldrich, product number 1.11355), and a correlation coefficient (R^2) of ≥ 0.9999 was achieved; the instrumental detection limit for Pb was 0.01 mg L^{-1}. Procedural blanks and duplicate samples were included in each analytical batch to monitor contamination and method precision. All extractions and ICP-OES measurements were conducted in triplicate, and the results are presented as means and standard deviations.

Geophysical surveys and data processing

ERT and TDIP surveys were performed in O-M and S-M plots on the same days as the soil sampling events. Measurements were performed with a Syscal Pro resistivity/IP system (IRIS Instruments, Orléans, France) using a dipole–dipole array of 39 silver electrodes (purity > 99%) spaced at 0.1 m along the central line of each plot (A–A′ in Fig. 1c; line length 3.8 m). Current was injected for 2 s at 200 V (T_1 and T_2) or 400 V (T_3), and each reading was stacked twice. Readings with non-positive apparent resistivity, stacking deviation above 5%, injected current below 1 mA, or invalid decay record were removed before inversion, together with apparent resistivity outliers deviating by more than 0.5 $\log_{10}$ units from the median of readings with the same dipole length and separation.

Two-dimensional resistivity and chargeability models were obtained with pyGIMLi version 1.6.0 (Rücker et al., 2017) on an unstructured triangular mesh with a cell size of approximately 3 cm, using smoothness-constrained regularization and robust (L1-norm) data weighting; the same mesh and settings were applied to all surveys. T_1 data of each plot were

inverted independently, and T_2 and T_3 data were inverted with T_1 model as the starting and reference model (Dimech et al., 2022). Chargeability (m) models were obtained by a linearized inversion based on the corresponding resistivity model. For each model cell, M_N (mS m^{-1}) was calculated as m divided by resistivity (ρ); M_N was used as the main IP parameter because it is proportional to the quadrature conductivity and reflects interfacial polarization with less influence of electrolytic conduction than m (Lesmes and Frye, 2001; Slater and Lesmes, 2002). Temporal changes were expressed as cell-by-cell ratios relative to T_1. Inversion settings and data misfits are summarized in Supplementary Table S2. Depth profiles (Fig. 7) were derived from the model cells located between 1.0 and 2.8 m along A–A′ as the median and the 25th–75th percentile range in 0.1-m depth intervals; ratio profiles were computed from the cell-by-cell ratios.

References

Abdilla, B., Lee, S. S., Fenter, P. & Sturchio, N. C. Dynamic inhibition of calcite dissolution in flowing acidic Pb^{2+} solutions. Environ. Sci. Technol. 58, 7133–7143 (2024). https://doi.org/10.1021/acs.est.3c10105

Ahmad, M., Hashimoto, Y., Moon, D. H., Lee, S. S. & Ok, Y. S. Immobilization of lead in a Korean military shooting range soil using eggshell waste: an integrated mechanistic approach. J. Hazard. Mater. 209–210, 392–401 (2012). https://doi.org/10.1016/j.jhazmat.2012.01.047

Ahn, Y., Han, M. & Choi, J. Monitoring the mobility of heavy metals and risk assessment in mine-affected soils after stabilization. J. Hazard. Mater. 400, 123231 (2020). https://doi.org/10.1016/j.jhazmat.2020.123231

Ahn, Y., Han, M. & Choi, J. Effect of electrode types and soil moisture on the application of electrical resistivity tomography and time-domain induced polarization for monitoring soil stabilization. Measurement 187, 110220 (2022). https://doi.org/10.1016/j.measurement.2021.110220

Bian, R. et al. A three-year experiment confirms continuous immobilization of cadmium and lead in contaminated paddy field with biochar amendment. J. Hazard. Mater. 272, 121–128 (2014). https://doi.org/10.1016/j.jhazmat.2014.03.017

Bolan, N. et al. Remediation of heavy metal(loid)s contaminated soils – to mobilize or to immobilize? J. Hazard. Mater. 266, 141–166 (2014). https://doi.org/10.1016/j.jhazmat.2013.12.018

Breede, K. et al. Spectral induced polarization measurements on variably saturated sand–clay mixtures. Near Surf. Geophys. 10, 479–489 (2012). https://doi.org/10.3997/1873-0604.2012048

Cao, X., Ma, L. Q., Chen, M., Hardison, D. W. Jr & Harris, W. G. Weathering of lead bullets and their environmental effects at outdoor shooting ranges. J. Environ. Qual. 32, 526–534 (2003a). https://doi.org/10.2134/jeq2003.5260

Cao, X., Ma, L. Q., Chen, M., Hardison, D. W. & Harris, W. G. Lead transformation and distribution in the soils of shooting ranges in Florida, USA. Sci. Total Environ. 307, 179–189 (2003b). https://doi.org/10.1016/S0048-9697(02)00543-0

Chen, L., Du, Y.-J., Liu, S.-Y. & Jin, F. Evaluation of cement hydration properties of cement-stabilized lead-contaminated soils using electrical resistivity measurement. J. Hazard. Toxic Radioact. Waste 15, 312–320 (2011). https://doi.org/10.1061/(ASCE)HZ.1944-8376.0000073

Chen, Q. Y., Tyrer, M., Hills, C. D., Yang, X. M. & Carey, P. Immobilisation of heavy metal in cement-based solidification/stabilisation: a review. Waste Manag. 29, 390–403 (2009). https://doi.org/10.1016/j.wasman.2008.01.019

Choi, S. H. et al. Toward transformation of bivalve shell wastes into high value-added and sustainable products in South Korea: a review. J. Ind. Eng. Chem. 129, 38–52 (2024). https://doi.org/10.1016/j.jiec.2023.08.032

614 Cui, H. et al. Leachability, availability and bioaccessibility of Cu and Cd in a contaminated
615 soil treated with apatite, lime and charcoal: a five-year field experiment. Ecotoxicol.
616 Environ. Saf. 134, 148–155 (2016). https://doi.org/10.1016/j.ecoenv.2016.07.005
617 Dimech, A. et al. A review on applications of time-lapse electrical resistivity tomography
618 over the last 30 years: perspectives for mining waste monitoring. Surv. Geophys. 43,
619 1699–1759 (2022). https://doi.org/10.1007/s10712-022-09731-2
620 Farshadirad, A., Hosseinpur, A. R., Motaghian, H. R. & Ghorbani Dashtaki, S. Zn
621 fractionation and availability in different soil aggregate fractions from Isfahan region,
622 Central Iran. Arch. Agron. Soil Sci. 63, 1419–1430 (2017).
623 https://doi.org/10.1080/03650340.2017.1280729
624 Feng, M.-H., Shan, X.-Q., Zhang, S.-Z. & Wen, B. Comparison of a rhizosphere-based
625 method with other one-step extraction methods for assessing the bioavailability of soil
626 metals to wheat. Chemosphere 59, 939–949 (2005).
627 https://doi.org/10.1016/j.chemosphere.2004.11.056
628 Fjellvåg, H., Grønvold, F., Stølen, S. & Hauback, B. On the crystallographic and magnetic
629 structures of nearly stoichiometric iron monoxide. J. Solid State Chem. 124, 52–57
630 (1996). https://doi.org/10.1006/jssc.1996.0206
631 Fleet, M. E. The structure of magnetite. Acta Crystallogr. B 37, 917–920 (1981).
632 https://doi.org/10.1107/S0567740881004597
633 Grubb, D. G., Jagupilla, S. C., Cummings, R. & Wazne, M. Immobilization of lead, tungsten,
634 and phosphate by steel slag fines: metals thresholding and rate studies. J. Hazard. Toxic
635 Radioact. Waste 18, 04014017 (2014). https://doi.org/10.1061/(ASCE)HZ.2153-
636 5515.0000214
637 Halim, C. E., Amal, R., Beydoun, D., Scott, J. A. & Low, G. Evaluating the applicability of a
638 modified toxicity characteristic leaching procedure (TCLP) for the classification of
639 cementitious wastes containing lead and cadmium. J. Hazard. Mater. 103, 125–140
640 (2003). https://doi.org/10.1016/S0304-3894(03)00245-0
641 Hao, N. et al. Content and morphology of lead remediated by activated carbon and biochar: a
642 spectral induced polarization study. J. Hazard. Mater. 411, 124605 (2021).
643 https://doi.org/10.1016/j.jhazmat.2020.124605
644 Jiang, Q. et al. Solidification/stabilization of soil heavy metals by alkaline industrial wastes: a
645 critical review. Environ. Pollut. 312, 120094 (2022).
646 https://doi.org/10.1016/j.envpol.2022.120094
647 Kumpiene, J., Lagerkvist, A. & Maurice, C. Stabilization of As, Cr, Cu, Pb and Zn in soil
648 using amendments – a review. Waste Manag. 28, 215–225 (2008).
649 https://doi.org/10.1016/j.wasman.2006.12.012
650 Lee, C. H., Lee, D. K., Ali, M. A. & Kim, P. J. Effects of oyster shell on soil chemical and
651 biological properties and cabbage productivity as a liming materials. Waste Manag. 28,
652 2702–2708 (2008). https://doi.org/10.1016/j.wasman.2007.12.005
653 Lee, S.-J., Han, M. H., Ahn, Y.-T., Jeon, B.-H. & Choi, J. Assessment of effectiveness in
654 stabilization/solidification of arsenic-contaminated soil: long-term leaching test and

655 geophysical measurement. Environ. Sci. Pollut. Res. 30, 120472–120482 (2023).
656 https://doi.org/10.1007/s11356-023-30641-2
657 Lee, S., Kim, M., Lee, N., Ahn, Y. & Choi, J. Integrated geochemical and geophysical
658 assessment for monitoring soil stabilization with waste oyster shells. Sci. Rep. 15, 37110
659 (2025). https://doi.org/10.1038/s41598-025-21141-z
660 Lee, S.-J. et al. Development and validation of a statistical prediction model for estimating
661 soil lead contamination in a sloped shooting range zone using geochemical and
662 geophysical data. J. Hazard. Mater. Adv. 18, 100760 (2025).
663 https://doi.org/10.1016/j.hazadv.2025.100760
664 Lesmes, D. P. & Frye, K. M. Influence of pore fluid chemistry on the complex conductivity
665 and induced polarization responses of Berea sandstone. J. Geophys. Res. Solid Earth 106,
666 4079–4090 (2001). https://doi.org/10.1029/2000JB900392
667 Lévy, L. et al. Quantifying reagent spreading by cross-borehole electrical tomography to
668 assess performance of groundwater remediation. Water Resour. Res. 58,
669 e2022WR032218 (2022). https://doi.org/10.1029/2022WR032218
670 Li, Y., Jia, S. & Liu, J. Solidification, remediation and long-term stability of heavy metal
671 contaminated soil under the background of sustainable development. Sci. Rep. 12, 10330
672 (2022). https://doi.org/10.1038/s41598-022-14122-z
673 Liu, L., Li, W., Song, W. & Guo, M. Remediation techniques for heavy metal-contaminated
674 soils: principles and applicability. Sci. Total Environ. 633, 206–219 (2018).
675 https://doi.org/10.1016/j.scitotenv.2018.03.161
676 Liu, J. et al. Mechanism of stabilized/solidified heavy metal contaminated soils with cement-
677 fly ash based on electrical resistivity measurements. Measurement 141, 85–94 (2019).
678 https://doi.org/10.1016/j.measurement.2019.03.070
679 Liu, X. et al. Study on the strength, leachability, and electrical resistivity of lead-
680 contaminated soil solidified with a slag-based binder. Bull. Eng. Geol. Environ. 80, 8553–
681 8564 (2021). https://doi.org/10.1007/s10064-021-02453-6
682 Markgraf, S. A. & Reeder, R. J. High-temperature structure refinements of calcite and
683 magnesite. Am. Mineral. 70, 590–600 (1985).
684 Martinho, E. Electrical resistivity and induced polarization methods for environmental
685 investigations: an overview. Water Air Soil Pollut. 234, 215 (2023).
686 https://doi.org/10.1007/s11270-023-06214-x
687 Merritt, A. J. et al. Measurement and modelling of moisture–electrical resistivity relationship
688 of fine-grained unsaturated soils and electrical anisotropy. J. Appl. Geophys. 124, 155–
689 165 (2016). https://doi.org/10.1016/j.jappgeo.2015.11.005
690 Ministry of Environment of Korea. Enforcement Rule of the Soil Environment Conservation
691 Act, Annex 7: Soil contamination countermeasure standards (Article 20). National Law
692 Information Center https://www.law.go.kr (2018).
693 Moon, D. H. et al. Stabilization of lead and copper contaminated firing range soil using
694 calcined oyster shells and fly ash. Environ. Geochem. Health 35, 705–714 (2013).
695 https://doi.org/10.1007/s10653-013-9528-9

Moon, D. H. et al. Stabilization of As-, Pb-, and Cu-contaminated soil using calcined oyster shells and steel slag. Environ. Sci. Pollut. Res. 22, 11162–11169 (2015). https://doi.org/10.1007/s11356-015-4612-6

Ok, Y. S., Lim, J. E. & Moon, D. H. Stabilization of Pb and Cd contaminated soils and soil quality improvements using waste oyster shells. Environ. Geochem. Health 33, 83–91 (2011). https://doi.org/10.1007/s10653-010-9329-3

Porter, S. K., Scheckel, K. G., Impellitteri, C. A. & Ryan, J. A. Toxic metals in the environment: thermodynamic considerations for possible immobilization strategies for Pb, Cd, As, and Hg. Crit. Rev. Environ. Sci. Technol. 34, 495–604 (2004). https://doi.org/10.1080/10643380490492412

Redhammer, G. J., Tippelt, G., Roth, G. & Amthauer, G. Structural variations in the brownmillerite series $Ca_2(Fe_{2-x}Al_x)O_5$: single-crystal X-ray diffraction at 25 °C and high-temperature X-ray powder diffraction (25 °C ≤ T ≤ 1000 °C). Am. Mineral. 89, 405–420 (2004). https://doi.org/10.2138/am-2004-2-322

Revil, A. & Glover, P. W. J. Nature of surface electrical conductivity in natural sands, sandstones, and clays. Geophys. Res. Lett. 25, 691–694 (1998). https://doi.org/10.1029/98GL00296

Revil, A. & Skold, M. Salinity dependence of spectral induced polarization in sands and sandstones. Geophys. J. Int. 187, 813–824 (2011). https://doi.org/10.1111/j.1365-246X.2011.05181.x

Revil, A., Karaoulis, M., Johnson, T. & Kemna, A. Review: some low-frequency electrical methods for subsurface characterization and monitoring in hydrogeology. Hydrogeol. J. 20, 617–658 (2012). https://doi.org/10.1007/s10040-011-0819-x

Rücker, C., Günther, T. & Wagner, F. M. pyGIMLi: an open-source library for modelling and inversion in geophysics. Comput. Geosci. 109, 106–123 (2017). https://doi.org/10.1016/j.cageo.2017.07.011

Saneiyan, S., Ntarlagiannis, D., Werkema, D. D. Jr & Ustra, A. Geophysical methods for monitoring soil stabilization processes. J. Appl. Geophys. 148, 234–244 (2018). https://doi.org/10.1016/j.jappgeo.2017.12.008

Shen, Z., Jin, F., O'Connor, D. & Hou, D. Solidification/stabilization for soil remediation: an old technology with new vitality. Environ. Sci. Technol. 53, 11615–11617 (2019). https://doi.org/10.1021/acs.est.9b04990

Slater, L. D. & Lesmes, D. IP interpretation in environmental investigations. Geophysics 67, 77–88 (2002). https://doi.org/10.1190/1.1451353

Slater, L., Ntarlagiannis, D. & Wishart, D. On the relationship between induced polarization and surface area in metal-sand and clay-sand mixtures. Geophysics 71, A1–A5 (2006). https://doi.org/10.1190/1.2187707

Song, Y., Shi, X., Meng, Y., Qiang, S. & Du, X. Monitoring cadmium remediation in biochar-amended porous media using spectral induced polarization. J. Appl. Geophys. 251, 106328 (2026). https://doi.org/10.1016/j.jappgeo.2026.106328

736 Sorvari, J., Antikainen, R. & Pyy, O. Environmental contamination at Finnish shooting
737 ranges—the scope of the problem and management options. Sci. Total Environ. 366, 21–
738 31 (2006). https://doi.org/10.1016/j.scitotenv.2005.12.019
739 Spence, R. D. & Shi, C. (eds) Stabilization and Solidification of Hazardous, Radioactive, and
740 Mixed Wastes (CRC Press, 2005).
741 Taylor, H. F. W. Cement Chemistry 2nd edn (Thomas Telford, 1997).
742 Tessier, A., Campbell, P. G. C. & Bisson, M. Sequential extraction procedure for the
743 speciation of particulate trace metals. Anal. Chem. 51, 844–851 (1979).
744 https://doi.org/10.1021/ac50043a017
745 Tsurumi, T., Hirano, Y., Kato, H., Kamiya, T. & Daimon, M. Crystal structure and hydration
746 of belite. Ceram. Trans. 40, 19–25 (1994).
747 Ulrich, C. & Slater, L. Induced polarization measurements on unsaturated, unconsolidated
748 sands. Geophysics 69, 762–771 (2004). https://doi.org/10.1190/1.1759462
749 US EPA. Treatment Technologies for Site Cleanup: Annual Status Report 12th edn. Report
750 EPA-542-R-07-012 (U.S. Environmental Protection Agency, Office of Solid Waste and
751 Emergency Response, 2007).
752 US EPA. Toxicity characteristic. Code of Federal Regulations, Title 40, § 261.24 (55 FR
753 11862, 29 Mar 1990, as amended); https://www.ecfr.gov/current/title-40/chapter-
754 I/subchapter-I/part-261/subpart-C/section-261.24
755 Weller, A., Slater, L., Nordsiek, S. & Ntarlagiannis, D. On the estimation of specific surface
756 per unit pore volume from induced polarization: a robust empirical relation fits multiple
757 data sets. Geophysics 75, WA105–WA112 (2010). https://doi.org/10.1190/1.3471577
758 Wu, Y., Hubbard, S., Williams, K. H. & Ajo-Franklin, J. On the complex conductivity
759 signatures of calcite precipitation. J. Geophys. Res. Biogeosci. 115, G00G04 (2010).
760 https://doi.org/10.1029/2009JG001129
761 Wu, Y., Slater, L., Versteeg, R. & LaBrecque, D. A comparison of the low frequency
762 electrical signatures of iron oxide versus calcite precipitation in granular zero valent iron
763 columns. J. Contam. Hydrol. 95, 154–167 (2008).
764 https://doi.org/10.1016/j.jconhyd.2007.09.003
765 Xia, T. et al. The evolving roles of electrical geophysical methods for in situ remediation
766 assessment: progress and perspectives. Water Resour. Res. 62, e2025WR043172 (2026).
767 https://doi.org/10.1029/2025WR043172
768 Xu, D.-M., Fu, R.-B., Wang, J.-X., Shi, Y.-X. & Guo, X.-P. Chemical stabilization
769 remediation for heavy metals in contaminated soils on the latest decade: available
770 stabilizing materials and associated evaluation methods—a critical review. J. Clean. Prod.
771 321, 128730 (2021). https://doi.org/10.1016/j.jclepro.2021.128730
772 Xue, Z.-F. et al. Investigating immobilization efficiency of Pb in solution and loess soil using
773 bio-inspired carbonate precipitation. Environ. Pollut. 322, 121218 (2023).
774 https://doi.org/10.1016/j.envpol.2023.121218
775 Yang, Y.-X., Meng, L.-L., Zhou, S., Xia, M. & Bate, B. The physicochemical interacting
776 mechanisms and real-time spectral induced polarization monitoring of lead remediation

by an aeolian soil. J. Hazard. Mater. 474, 134744 (2024). https://doi.org/10.1016/j.jhazmat.2024.134744

Yildirim, I. Z. & Prezzi, M. Chemical, mineralogical, and morphological properties of steel slag. Adv. Civ. Eng. 2011, 463638 (2011). https://doi.org/10.1155/2011/463638

Yu, S., He, Z. L., Huang, C. Y., Chen, G. C. & Calvert, D. V. Copper fractionation and extractability in two contaminated variable charge soils. Geoderma 123, 163–175 (2004). https://doi.org/10.1016/j.geoderma.2004.02.003

Zhou, S. et al. Monitoring of copper adsorption on biochar using spectral induced polarization method. Environ. Res. 251, 118778 (2024). https://doi.org/10.1016/j.envres.2024.118778

Data availability

The datasets generated and analyzed during the current study are available from the corresponding author on reasonable request.

Acknowledgements

This research was supported by the institutional program (No. 26Z9071) of the Korea Institute of Science and Technology (KIST).

The research for this paper was carried out under the KICT Research Program (Project no. 20260161–001, Development of Digital Urban Flood Control Technology for the Realization of Flood Safety City) funded by the Ministry of Science and ICT.

Author contributions

S.J.L. collected and analyzed the data, contributed to the conceptualization of the study, and drafted the manuscript. N.R.L. contributed to the preparation of figures. S.L.Y. critically reviewed and revised the manuscript. J.Y.C. designed the study, supervised the research, and critically reviewed and revised the manuscript. All authors reviewed and approved the final manuscript.

Competing interests

The authors declare no competing interests

Figure legends

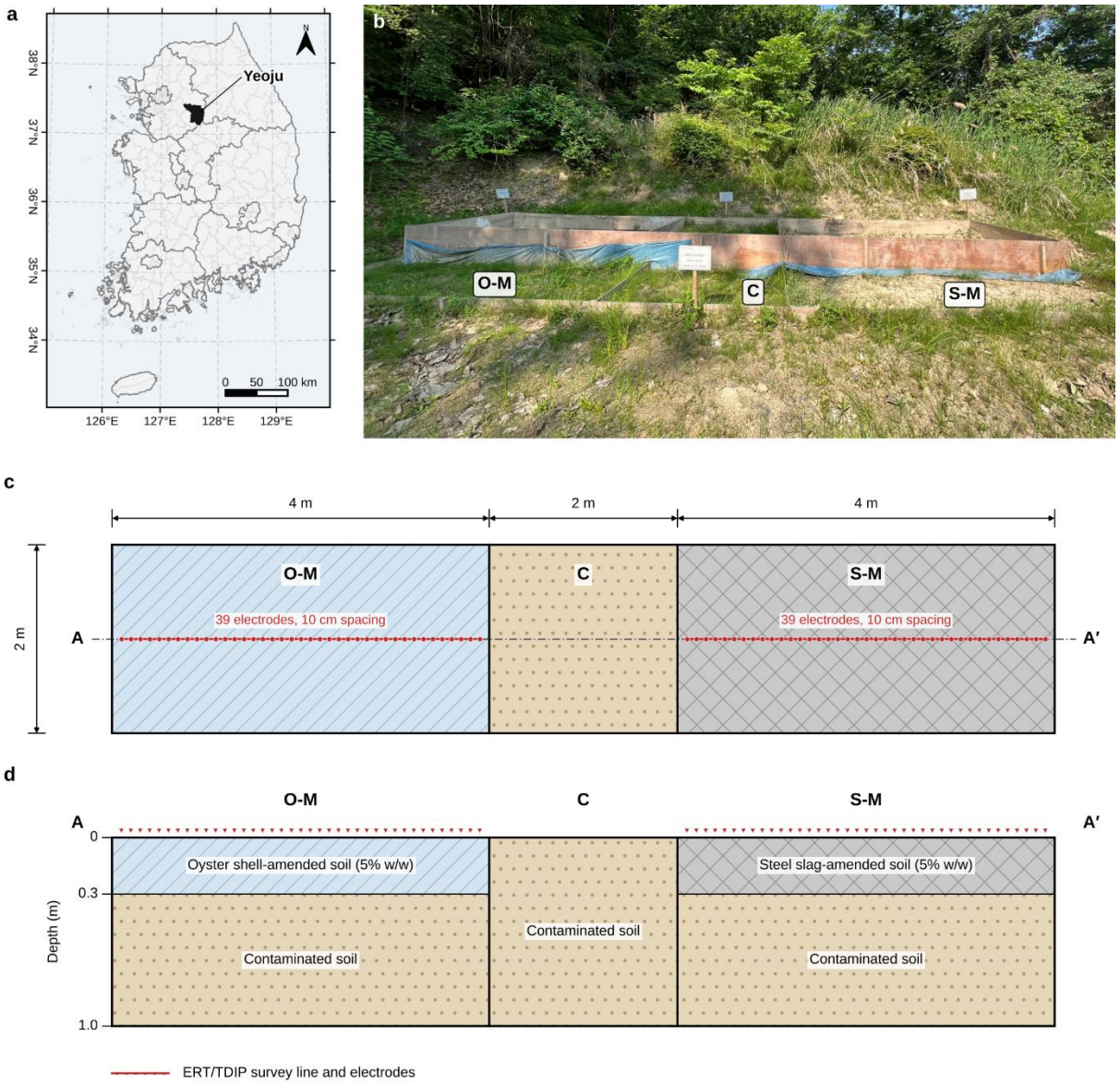
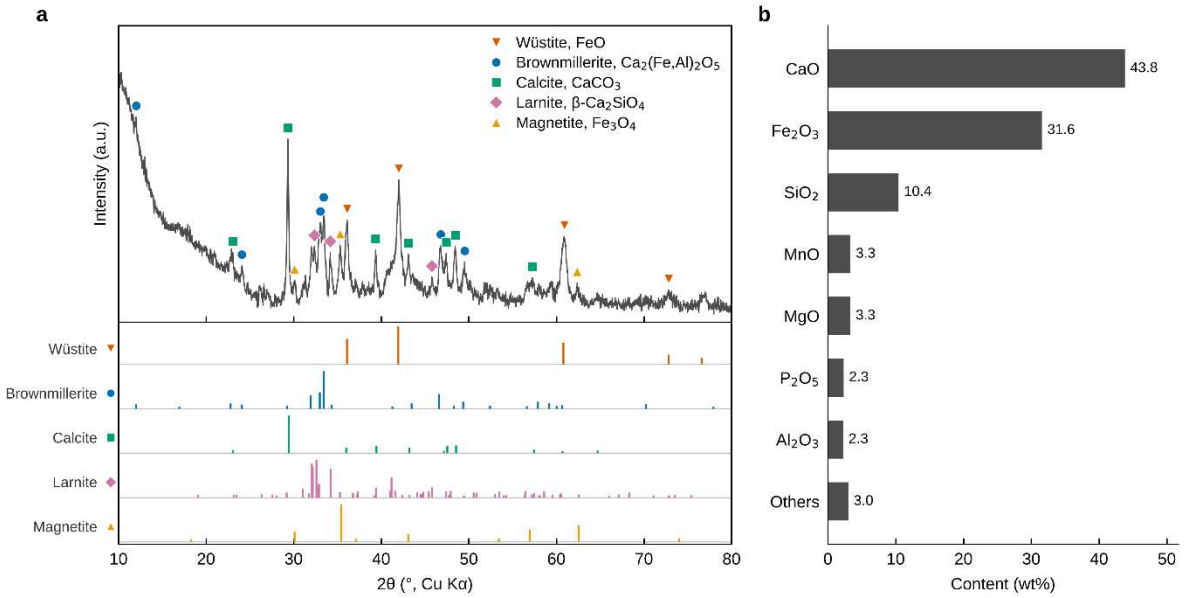


Fig. 1 Study site and test-plot design. (**a**) Location of Yeoju, Republic of Korea (map produced with QGIS 4.2.3); (**b**) Test plots at the study site; (**c**) Plan view of the test plots; (**d**) Cross-section along A–A′. In the oyster shell-mixed plot (O-M) and the steel slag-mixed plot (S-M), contaminated soil mixed with 5% (w/w) oyster shell or steel slag, respectively, was placed as a 0.3-m-thick cover over the contaminated soil, giving a total soil depth of 1 m. The control plot (C) contained only contaminated soil to a depth of 1 m and was used for chemical monitoring. Electrical resistivity tomography/time-domain induced polarization (ERT/TDIP) surveys were conducted along A–A′ in O-M and S-M using 39 electrodes at 10-cm spacing.



821

822 **Fig. 2** Characterization of the steel slag. (**a**) X-ray diffraction (XRD) pattern (Cu Kα) with
823 phase identification. Reference patterns (bottom) were calculated from the crystal structures of
824 wüstite (Fjellvåg et al., 1996), brownmillerite (Redhammer et al., 2004), calcite (Markgraf and
825 Reeder, 1985), larnite (Tsurumi et al., 1994), and magnetite (Fleet, 1981); (**b**) Major oxide
826 composition determined by X-ray fluorescence (XRF)—oxides below 1 wt% are grouped as
827 Others.

828

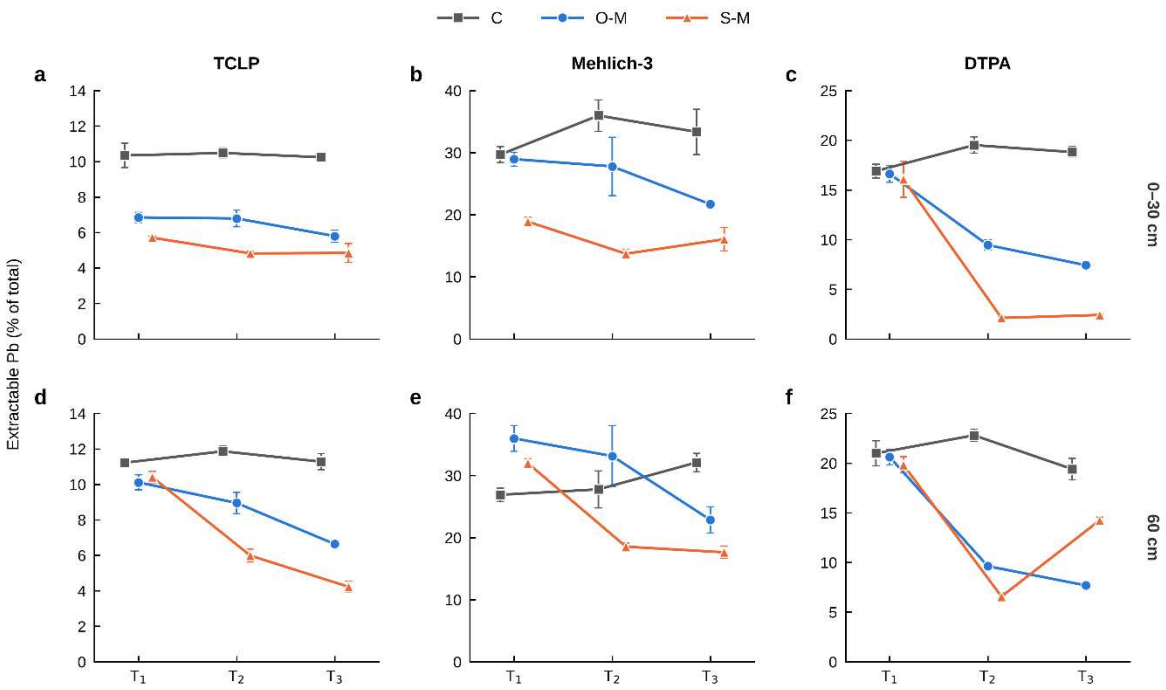
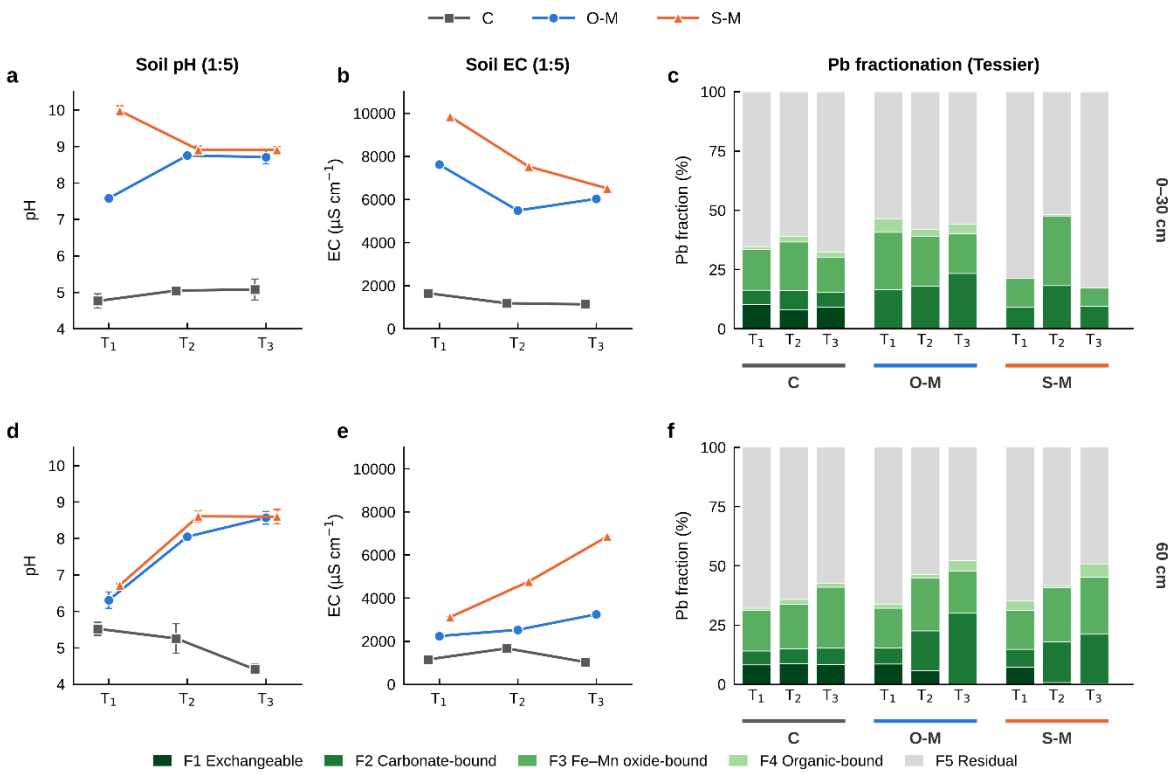


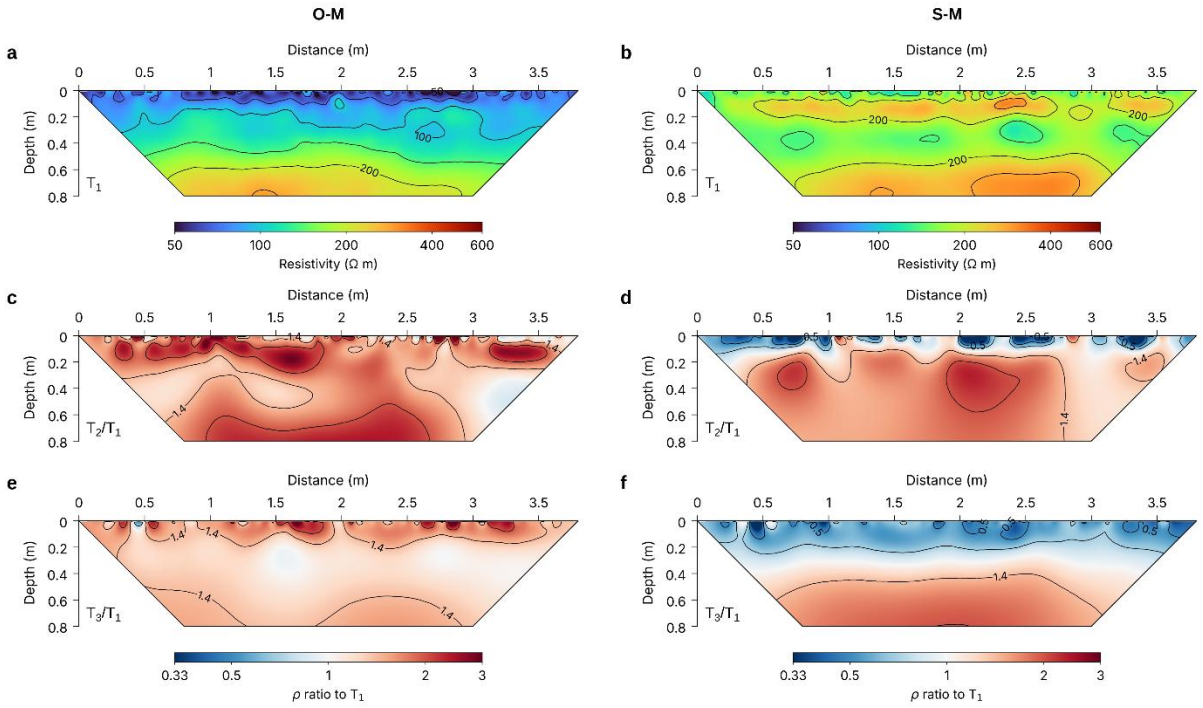
Fig. 3 Extractable Pb in the test-plot soils. Pb extracted by (**a**, **d**) toxicity characteristic leaching procedure (TCLP), (**b**, **e**) Mehlich-3 and (**c**, **f**) diethylenetriaminepentaacetic acid (DTPA), expressed as a percentage of the total Pb of the same sample, at (**a**–**c**) 0–30 cm and (**d**–**f**) 60 cm depth. In O-M and S-M, the 0–30 cm layer corresponds to the amended layer. Sampling dates: T_1, 15 September 2021; T_2, 14 June 2022; T_3, 17 October 2022. Values are means ± SD of triplicate extractions. C, control plot; O-M, oyster shell-mixed plot; S-M, steel slag-mixed plot.



838

839 **Fig. 4** Soil pH, electrical conductivity (EC), and Pb fractionation in the test plots. (**a**, **d**) Soil
840 pH and (**b**, **e**) EC, both measured at a soil-to-water ratio of 1:5, and (**c**, **f**) Pb fractions
841 determined by the Tessier sequential extraction, at (**a**–**c**) 0–30 cm and (**d**–**f**) 60 cm depth. pH
842 and EC are means of duplicate measurements, with bars indicating the range. Pb fractions (F1,
843 exchangeable; F2, carbonate-bound; F3, Fe–Mn oxide-bound; F4, organic-bound; F5, residual)
844 are means of triplicate extractions, expressed as a percentage of the sum of F1–F5. Sampling
845 dates and plot abbreviations as in Fig. 3.

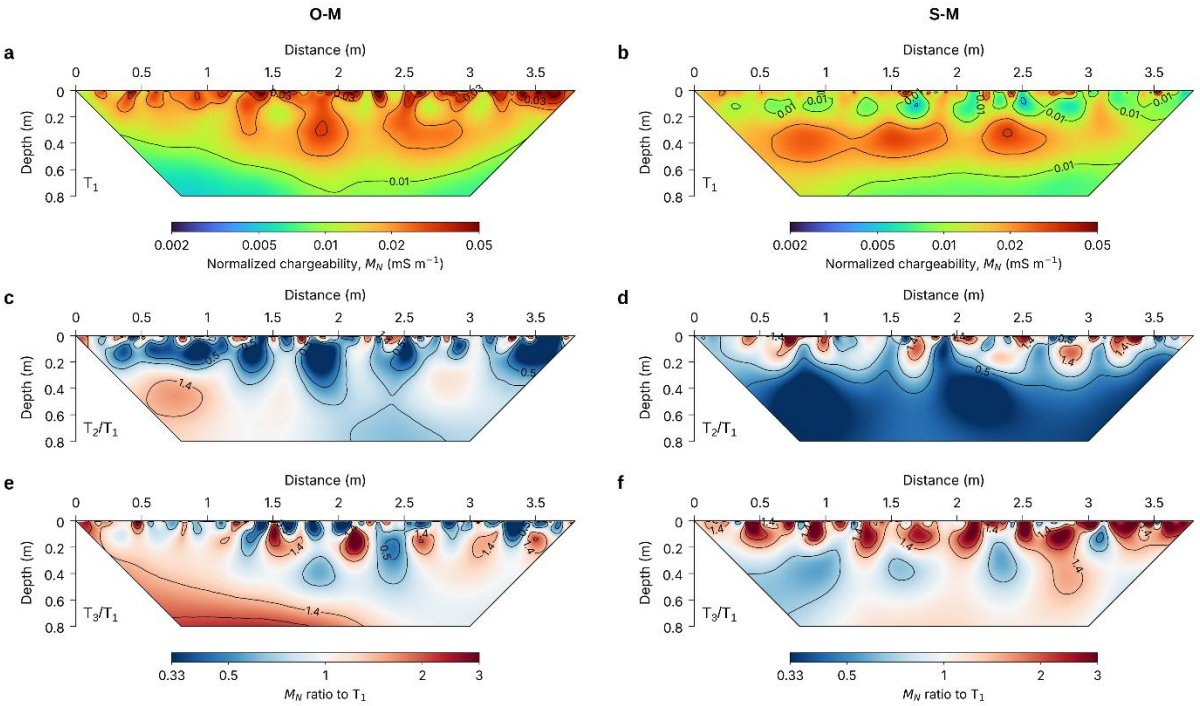
846



847

848 **Fig. 5** Electrical resistivity sections of the O-M (**a**, **c**, **e**) and S-M (**b**, **d**, **f**) plots. (**a**, **b**) Inverted
849 resistivity at T_1; (**c**, **d**) Ratio of resistivity at T_2 to that at T_1; (**e**, **f**) Ratio of resistivity at T_3 to
850 that at T_1. Data from T_2 and T_3 were inverted using the T_1 model as the reference model, and
851 ratios were calculated cell by cell. Black lines are contours at the labelled values. Color scales
852 are logarithmic. Survey dates as in Fig. 3.

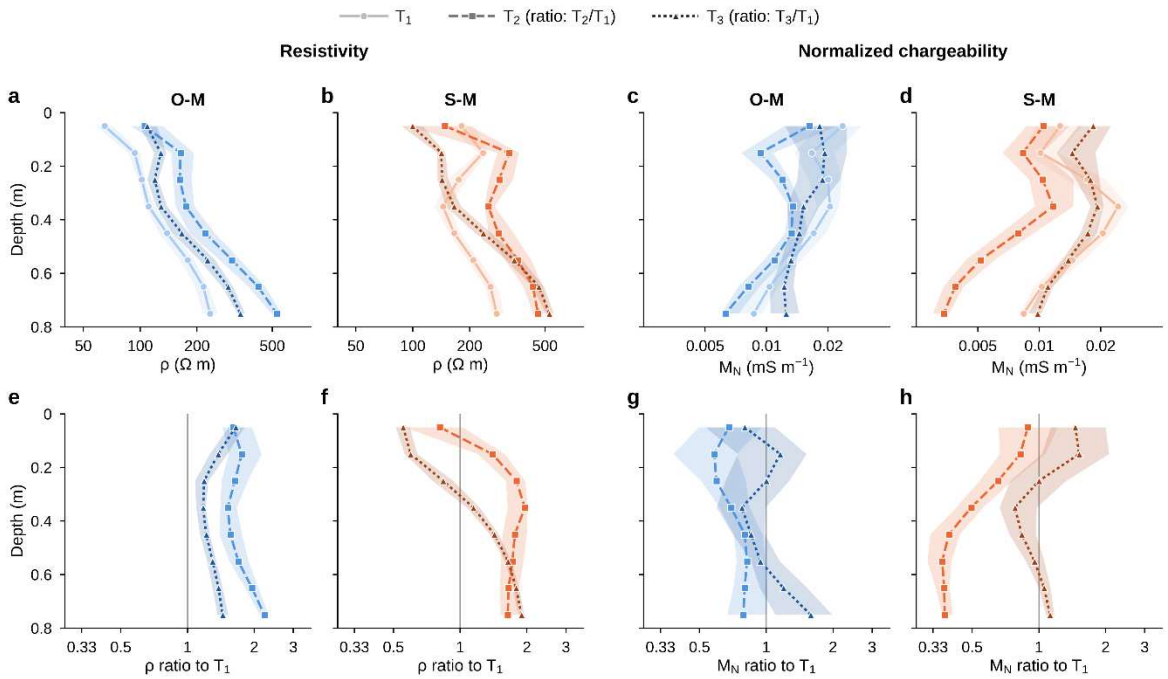
853



854

855 **Fig. 6** Normalized chargeability (M_N) sections of the O-M (**a**, **c**, **e**) and S-M (**b**, **d**, **f**) plots. (**a**,
856 **b**) M_N at T_1; (**c**, **d**) Ratio of M_N at T_2 to that at T_1; (**e**, **f**) Ratio of M_N at T_3 to that at T_1. M_N was
857 calculated as the inverted chargeability divided by the inverted resistivity of each model cell.
858 Inversion, ratio calculation, contours, and color scales as in Fig. 5.

859



860

861 **Fig. 7.** Depth profiles of resistivity and normalized chargeability (M_N) in the O-M and S-M
862 plots. (**a**–**d**) Values at T_1, T_2, and T_3: resistivity in (**a**) O-M and (**b**) S-M, and M_N in (**c**) O-M
863 and (**d**) S-M. (**e**–**h**) Ratios to T_1 (T_2/T_1 and T_3/T_1) for the same variables and plots as in (**a**–**d**).
864 Profiles were taken from the inverted sections in Figs. 5 and 6 and include the model cells
865 between 1.0 and 2.8 m along A–A′. Lines represent the median of these cells in 0.1-m depth
866 intervals, and shaded bands the 25th–75th percentile range. Grey vertical lines in (**e**–**h**) mark a
867 ratio of 1. All horizontal axes are logarithmic. Sampling dates as in Fig. 3.

868

869 **Table 1.** Physicochemical properties of the test-plot soils.

Property	Unit	0–30 cm			60 cm		
		C	O-M	S-M	C	O-M	S-M
Sand[b]	%	75.1	75.4	75.2	70.2	75.4	71.5
Silt[b]	%	16.8	16.8	17.6	21.0	18.2	20.0
Clay[b]	%	8.1	7.9	7.2	8.8	6.4	8.5
Texture (USDA)[b]	–	Sandy loam					
pH (1:5)[a]	–	4.76	7.58	9.98	5.52	6.31	6.72
EC (1:5)[a]	μS cm^{-1}	1645	7615	9840	1150	2235	3115
TOC[b]	%	2.44	3.97	2.15	2.19	2.67	2.55
Total Pb[a]	mg kg^{-1}	3007 (80)	3487 (61)	4507 (75)	3551 (84)	4846 (74)	6015 (107)

870 C, control plot; O-M, oyster shell-mixed plot; S-M, steel slag-mixed plot. In O-M and S-M, the 0–30 cm layer is
871 the amended layer (contaminated soil mixed with 5% (w/w) stabilizer). EC, electrical conductivity; TOC, total
872 organic carbon.

873 [a]Measured on samples collected at T_1 (15 September 2021). pH and EC are means of duplicate measurements.
874 Total Pb was determined by aqua regia digestion (means of triplicates, with SD in parentheses). Korean soil
875 contamination countermeasure standard for Region 3: Pb 2,100 mg kg^{-1}.

876

Supplementary information (planned)

Supplementary Table S1. Gravimetric water content of the soil samples (plot × depth × sampling date; duplicates).

Supplementary Table S2. Inversion settings (mesh, regularization, error model) and data misfits (χ^2) of the electrical resistivity tomography (ERT) and time-domain induced polarization (TDIP) inversions.

Supplementary Table S3. Total Pb, synthetic precipitation leaching procedure (SPLP)-extractable Pb, and absolute Tessier fraction contents for all samples.

Supplementary Files

This is a list of supplementary files associated with this preprint. Click to download.

- Supplementary.docx